Sensitive optical free-space receiver architecture for coherent combining of deep-space communication signals through atmospheric turbulence

Research Article | Vol. 32, No. 25 / 2 Dec 2024 / Optics Express 44799
Optics EXPRESS

Sensitive optical free-space receiver architecture for coherent combining of deep-space communication signals through atmospheric turbulence

RASMUS LARSSON,* MAGNUS KARLSSON, AND PETER A. ANDREKSON

Photonics Laboratory, Department of Microtechnology and Nanoscience, Chalmers University of Technology, SE - 412 96 Gothenburg, Sweden
rasmus.larsson@chalmers.se

Abstract: High data rate optical deep space communication links for future space missions need large capture area receivers that can efficiently couple light into a single-mode fiber. Coherent detection is attractive as it offers both high spectral efficiency and sensitivity. Here, we numerically investigate two such large area receivers in the context of weak signal reception; the multi-aperture array and the multi-mode fiber-coupled receiver, together with optical coherent combining. We find that the number of speckles captured by the aperture should match the number of modes supported by the receiver-fiber for high efficiency and sensitivity. Using an optically preamplified dither-optical phase locked loop for tip-tilt, phase, and amplitude compensation, we predict that efficient reception of signals can be maintained down to -80 dBm of received power per mode for realistic atmospheric channels.

1. Introduction

In recent years, free-space optical communications for deep space has seen rapid development with several demonstrations of laser-based communications, like the moon-orbiting satellite to earth link in [1] (2013) and just recently, in 2023, a deep space to earth downlink from the Psyche mission in [2] at 80 times the distance to the moon.

The transition from radio frequency (RF) communication to optical in deep space is attractive as shorter wavelength data-transmission not only suffers from less diffraction losses but can also enable higher data rates [3]. For the current state-of-the-art RF communications from the Mars reconnaissance orbiter in [4], the roughly 10,000 times shorter wavelength of 1.55 µm used in optical communications could reduce the diffraction loss by a factor $10,000^2$, or 80 dB, if using same sized transmitter and receiver. Optical communications could thus be instrumental in overcoming the data-relay bottleneck of current deep space missions (e.g. a few Mb/s in [4]).

To fully exploit the potential benefit of optical communications the implemented receivers must be as sensitive as possible. Currently, receivers for deep space laser communications mainly rely on avalanche photo-detectors [5] or, recently, super-conducting nano-wire single photon detectors [6]. Their use in combination with power-efficient modulation such as pulse-position modulation have achieved the current lowest receiver sensitivities to date with 0.08 photons per bit (PPB) at a 14 kb/s data rate in [7] and 8 PPB at a ~ 0.8 Gb/s data rate in [8]. Although these receivers achieve highest sensitivity, the modest data rates demonstrated are limited by the few GHz of detector bandwidth available [9], together with the inefficient bandwidth use of PPM [10].

#539071 https://doi.org/10.1364/OE.539071
Journal © 2024 Received 9 Aug 2024; revised 30 Sep 2024; accepted 13 Oct 2024; published 25 Nov 2024

Optics EXPRESS

Another record-sensitivity was demonstrated in [11] at 1 PPB with a 10 Gb/s data rate, instead with the use of optically preamplified coherent detection. The use of coherent reception enables sensitive receivers together with bandwidth efficient modulation formats and high data rates, as has been repeatedly demonstrated in the field of optical fiber transmission. Therefore, to boost the speed of deep space communication links beyond what the use of single-photon detectors can achieve, coherent free-space reception provides an appealing solution, with high quality off-the-shelves components and instruments readily available.

For incoherent reception, e.g. using single-photon detectors, realizing a large receive-area is relatively simple as focusing the light onto a, usually, few mm^2 detector is manageable in practice. This contrasts the stringent alignment requirements on the receive-optics when focusing the light into a single-mode fiber (SMF), which amplify in proportion to aperture size, for standard coherent reception. In addition, when receiving through the turbulent atmosphere the focused spot size is broadened [12], effectively limiting how much power that can coupled into a SMF.

One method commonly employed in optical astronomy to mitigate turbulence effects is the use of adaptive optics (AO) [13]. The use of AO for fiber-coupling with a 1 m telescope has also been investigated in [14] and uses a MEMs deformable mirror that re-aligns the turbulence-perturbed optical wave phase-front to reach a diffraction-limited spot size. For increasingly weak received signal powers, larger receive-telescopes are required and while an AO-system can be accommodated with more micro-mirror actuators for efficient turbulence compensation the alignment issue for large telescope to fiber reception remains.

One way to alleviate the alignment for large-area telescopes is the use of multi-mode fiber (MMF) coupling combined with photonic lanterns (PLs) for separation into SMF [15], or an array of smaller telescopes which are individually SMF-coupled [16]. The received signal in the individual SMFs from either approach may then be combined either optically using 50/50-couplers as in [17–19] or digitally after coherent reception as studied in [16,20,21]. In the context of weak received powers where a large number of SMF-channels is expected, the digital combining approach becomes costly in terms of the number of coherent receivers required (same as number of channels). In addition, such digital coherent combining systems pay a penalty in combining efficiency when considered for real-time operation at low signal power [20].

To reach a large optical combining efficiency, amplitude, polarization and phase between channels must be aligned, where the latter poses the most challenging in practice [18]. However, in our previous work in [19], we demonstrated optical coherent combining of a 10 Gbaud, quadrature phase-shift keyed (QPSK) data signal received using four individual apertures with >97% efficiency at ≥ -80 dBm signal power per channel. While the demonstration targeted the compensation of phase fluctuations only, it shows great potential for the implementation of a multi-aperture receiver for sensitive coherent reception.

Here, we extend the study on optical coherent combining of weak signals for deep space to earth downlinks by numerically simulating both multi-aperture and multi-mode reception through the turbulent atmosphere. Subsequent optical combining using amplitude and phase compensation is simulated and verified experimentally using an adaptation of the setup in [19].

The specific scenario studied here is shown in Fig. 1, where a weak plane-wave signal, with an average intensity I_r, is received through the atmosphere from a distant transmitter (moon or beyond). Here, the final received power $P_r = I_r A_r \eta_r$ depends on the total receive-area A_r and the receiver efficiency η_r which incorporates fiber-coupling and coherent combining losses.

Based on the simulations, we determine the optimal receiver architecture w.r.t. aperture size D and fiber mode count N_f for reaching high receiver efficiency at as low received signal powers as possible for a given turbulence channel, characterized by Fried's coherence length r_0 [12]. In general, it was found that both multi-aperture and multi-mode reception, when optimized, provide similar performance with coherent combining. When also accounting for tip-tilt compensation of angle of arrival (AOA) fluctuations, multi-mode reception provided a few dB better sensitivity.

Optics EXPRESS

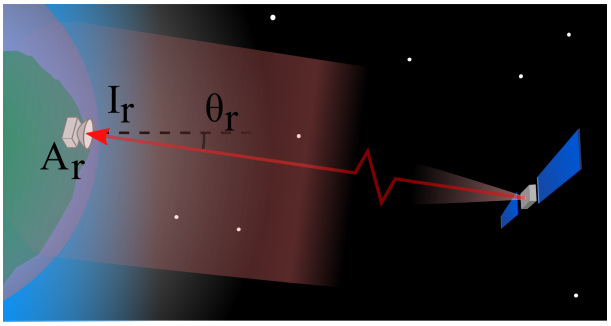

Fig. 1. The deep space downlink. A plane-wave signal is incident on the atmosphere and propagates to the receiver of area A_r at an angle θ_r to zenith.

In general, for any control system to compensate turbulence at a required bandwidth a minimum signal-to-noise ratio (SNR) is needed. For AO, multi-mode or multi-aperture reception, which compensates the de-correlation between many spatial modes or channels, it is convenient to specify the minimum SNR (or power) required per mode/channel, also known as the sensitivity. In [14], the minimum signal power to drive the AO-system was ~ -37 dBm for a 1 m diameter telescope (or ~ -61 dBm per mode to achieve $\eta_r = 0.5$, assuming 500 modes). In [19], a minimum power per channel of -70 dBm was needed to achieve >98% combining efficiency for a phase fluctuation strength of 51.3 rad/s. Likewise, in this study, we estimate the minimum power per mode/channel required to achieve η_r>0.5 on the order of -80 dBm for the investigated receivers when receiving with θ_r<60° angle to zenith at plausible high-altitude sites such as the La Palma and Manua Kea observatories.

In section 2 we provide an overview of the receiver system before focusing on its core parts, such as the free-space to fiber coupling efficiency in section 3, the tip-tilt-control for AOA fluctuations in section 4 and the coherent combining stage in section 5. In section 6 we discuss the total receiver efficiency for different architectures before a discussion and conclusion in section 7. Further details about models, simulations and experiment are provided in Supplement 1.

2. Complete model overview

In order to simulate the coherent combining performance, phase and amplitude variation statistics inside the different SMF channels are required. To obtain the power spectral densities (PSDs) of these fluctuations we relied on Monte Carlo-simulations of the optical field received by the SMFs.

The numerical simulation model for the receiver system can be categorized into three different parts: 1) atmospheric propagation from space to ground, 2) aperture to fiber reception and 3) the cascaded coherent combining system. These three stages to the receiver are illustrated in Fig. 2.

2.1. Stage 1

The atmospheric propagation in stage 1 is numerically simulated using the split-step beam propagation method described in [22] where the optical wave is sequentially propagated through free-space of constant refractive index and passed through discrete phase-screens that incorporates the random refractive-index variation. The phase screens are realized using the modified Von Karman atmospheric phase PSD (including sub-harmonics) with zero inner scale and infinite outer scale [23]. The Von Karman PSD depends on the refractive index structure parameter $C_n^2(z)$ which describe the strength of refractive-index variations at a position z along the propagation path. For space to ground propagation we used the Hufnagel-Valley model of the C_n^2-profile [24] with upper atmospheric rms wind speed of 21 m/s and a sea-level $C_n^2 = 1.7 \cdot 10^{-14}\,\mathrm{mm}^{-2/3}$ [25].

Optics EXPRESS

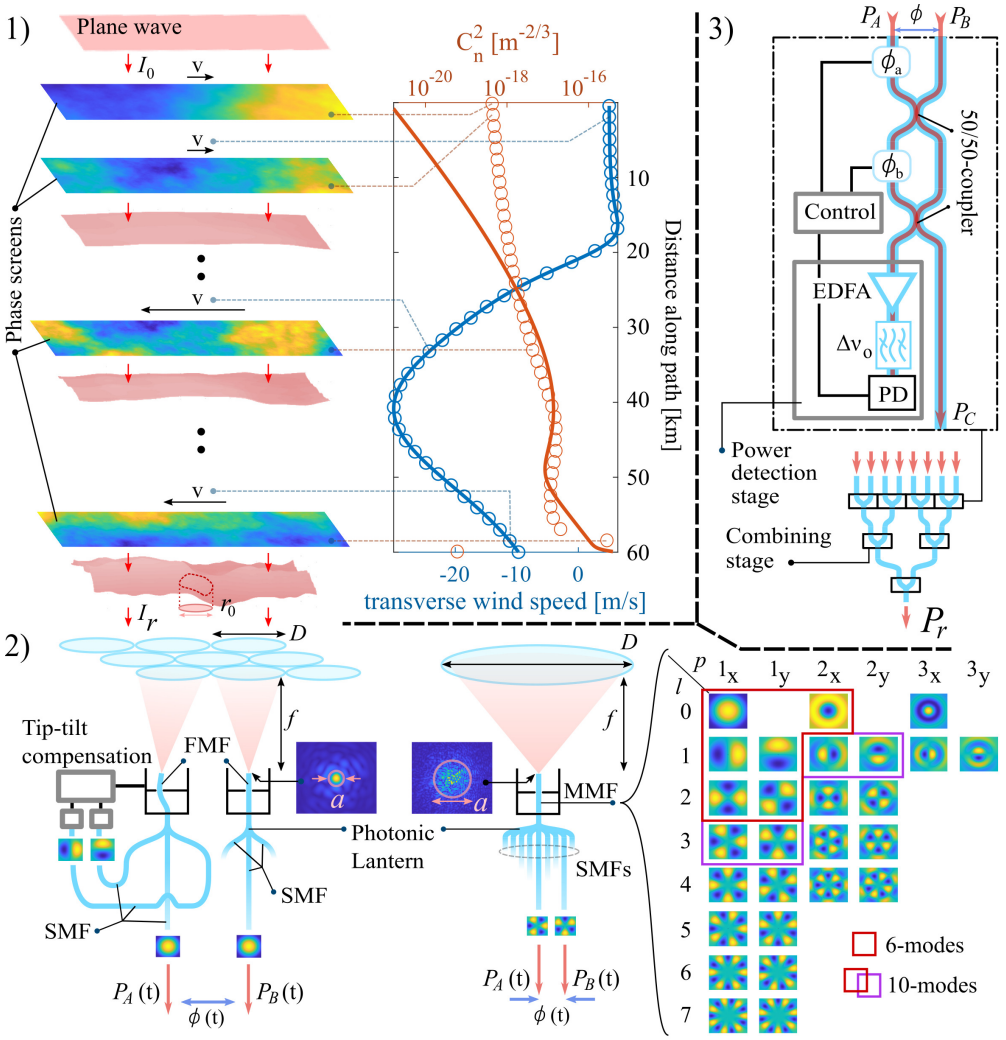

Fig. 2. The three stages to the system model. Stage 1) plane-wave propagation along a turbulent path through the atmosphere (modelled by solid C_n^2 and wind curves) using split-step beam propagation with discrete phase-screens (modelled by C_n^2 and wind circles). Stage 2) multi-aperture + single-mode reception, or single-aperture + multi-mode reception of the incident signal. With or without tip-tilt-control applied and using mode-selective photonic lanterns for separation into SMFs. Stage 3) coherent combining of SMF-signals using an optical phase locked loop with optically amplified error feedback using an EDFA, optical filter (bandwidth $\Delta\nu_0$) and photo-detector (PD). FMF: few-mode fiber.

An example of the C_n^2-profile of a $\theta_r = 60°$ slant path is shown in orange in Fig. 2. The phase screens (spaced equidistantly) were generated by matching moments of order 0,1,..,7 between a discrete-layer C_n^2-model, using 41 layers or more, to the continuous model. These are shown in orange rings in the figure and represent each phase screen in the propagation path.

The time-dynamic is incorporated in the simulation by continuously shifting the individual phase screens in the direction transverse to the propagation at a speed determined by the atmospheric wind speed at position z. This approach was used by Greenwood and Fried in [26] to predict bandwidth requirements for AO-systems [27]. Here, we use a Gaussian wind-speed

Optics EXPRESS

model as described in [28], with wind direction modelled by a super-Gaussian (see Supplement 1, sect. 2). An example of a typical atmospheric wind profile is shown in blue in the figure and each phase screen was shifted at the rate of the wind speed at its corresponding path position. Relative motion between transmitter, atmosphere and receiver adds to the phase-screen speed in principle, however, for a very distant transmitter this motion can be assumed negligible (for $\theta_r \leq 60°$).

Each simulation was realized for a duration of 1 s and at a 2 kHz sampling rate in time to capture the significant portion of the atmospheric time variation, typically limited to 1 kHz [29]. Meanwhile, the plane-wave starting field was modelled using a super-Gaussian of diameter 3-4.5 m with constant phase and intensity I_0. To avoid an exceptionally long simulation duration the field matrix size was chosen as 2^{11} or less which, in conjunction with required sampling conditions (described in [22]), limited the starting field size.

After atmospheric propagation, the field is characterized using Fried's coherence length r_0 [12], which depends on C_n^2 and provides an estimate of the static turbulence strength. The actual turbulence strength important to the control system also incorporates the wind speed, as suggested in [26], however, as most wind profiles considered here were similar, we refer to different turbulence cases using r_0. Meanwhile, the time-average received intensity I_r equals the initial intensity I_0 under a lossless atmosphere, something that can easily be adjusted if desired.

2.2. Stage 2

Stage 2 of the model is the receiver front-end and consists of one or an array of several focusing elements with aperture diameter D and focal length f. It is generally assumed here that coarse pointing is taken care of, with fine AOA fluctuations remaining to compensate. We consider the ideal case of a paraxial focusing system with a masking circular aperture. The numerical simulation of the focused field at the fiber interface (Supplement 1, sect. 3) is given by the spatial Fourier-transform of the aperture masked received field. The fiber-collected field is subsequently calculated via mode-overlap integrals between the focused field and the spatial modes of the fiber. The fiber was modelled as a step-index MMF with core diameter $a = 50\,\mu$m, core index $n_c = 1.462420$ and cladding index $n_g = 1.457420$ which for $\lambda = 1.55\,\mu$m featured a 0.1 numerical aperture and supported the 27 spatial LP-modes shown in the figure. The 6 and 10-mode subsets shown in the figure were also used to compare different mode-counts.

Both the single-aperture and multi-aperture receivers used the MMF but with different optimized focal lengths. In the multi-aperture receiver, only the fundamental mode of the MMF was used in subsequent coherent combining, prompting an optimized focal length that maximizes the power collected in this mode. This is equivalent to single-mode (SM) reception and is referred to as the SM-receiver. Here, f is optimized such that the diffraction-limited spot size ($\propto 1/D$) matches the fundamental mode profile, leading to $f \propto D$. The single-aperture MMF-reception case (referred to as the MM-receiver) is instead concerned with maximizing the power throughout all fiber modes. Here, f is optimized such that the turbulence-limited spot size $\propto 1/r_0$ matches the fundamental mode size, leading to $f \propto r_0$. Further details of the focal length optimization for both receivers are found in Supplement 1, sect. 3.

An example of a physical implementation of tip-tilt-control can be found in [30]. Similar to this, we equip our physical system model with mechanical control of the receive-fiber tip position in the focal plane of each focusing element to actively track the, due to AOA fluctuations, varying focus spot position to maximize fiber power coupling. The efficiency of this tip-tilt control is described by the tip-tilt efficiency $0 \leq \eta_{tt} \leq 1$ which accounts for the coupling loss due to imperfect tip-tilt compensation. To track the tip-tilt, two dither PLLs, one for each focal plane dimension (x and y), is applied in the model. We describe in Supplement 1, sect. 4B how the mechanical focal plane offset control can be seen as a phase control when normalized to the fiber core size. Practically, this system assumes fast and highly resolved mechanical control to

Optics EXPRESS

accommodate kHz level dither frequencies, something which can be enabled using piezo-electric actuation.

The feedback for the tip-tilt control is modelled differently for the SM and MM system. For the SM receiver, a few-mode fiber (FMF) for reception is used to feedback the optical error signal using the degenerate modes of $(l, p) = (1, 1)$ (see Fig. 2) which sense offset-variations of the focused spot in the x and y-directions, respectively. Using these higher order modes circumvents the need for tapping power off the fundamental mode which contains the important signal. For the MM receiver the tip-tilt-control was based on maximizing the final combined output power of stage 3 (tapped after optical amplification to avoid SNR loss of the communication signal), equivalent to maximizing the power captured across all modes of the MMF. Detection of the optical error signal used optical amplification, like for the combining stage, as will be discussed in stage 3). Further details on the tip-tilt control is included in Supplement 1, sect. 4.

It is furthermore assumed that each MMF-mode is perfectly separated into individual SMFs using a mode-selective PL for both receiver types. Such a PL, ideal for our investigated SM-receiver, has been physically realized in [31]. For the MM-receiver, mode-selectivity is mainly beneficial if the number of modes used for combining is smaller than the amount supported by the fiber as the power across, e.g., the LP-modes of the fiber, will be concentrated in the lower order modes [15] for weak turbulence cases (such as those discussed in this work).

2.3. Stage 3

After separation into SMFs, the signal is combined sequentially, two SMFs at a time in stage 3. As shown in Fig. 2, each pair of SMFs, carrying time varying powers P_A, P_B and relative phase ϕ, are input to a combining stage. The combining stage relies on two phase shifters ϕ_a and ϕ_b for compensation of phase and amplitude fluctuations respectively. This is the same system as in [19] but with an additional 3 dB coupler and phase shifter added. In detail, ϕ_a adjusts the relative phase between the two inputs such that they are 90° out of phase (exactly between constructive and destructive interference), resulting in equal power in both output ports of the first coupler. This is necessary to achieve perfect constructive interference on one output port in the secondary 50/50-coupler, which is ensured by appropriate phase control in ϕ_b (which will depend on the ratio P_A/P_B). The combined power P_C is related via the combining efficiency η as $P_C = \eta[P_A + P_B]$.

The control system is realized by using the destructive output port as feedback, whose power is the target of continuous minimization. The power detection stage for the destructive output, like in [19], includes optical amplification using an erbium-doped fiber amplifier (EDFA) (with noise figure = 3 dB) and optical filtering with a bandpass bandwidth $\Delta\nu_0 = 0.22$ nm before detection in a photo-detector. The use of optical amplification and filtering significantly improves the SNR and sensitivity of the control system which is now limited by amplified spontaneous emission noise (ASE) rather than thermal noise, see Supplement 1, sect. 4.

In a practical scenario, relative polarization and symbol delay between channels must also be controlled to achieve efficient combining. These aspects are more of practical concern however, as these effects are relatively stable compared to phase and can be accommodated using slow tracking which will not be fundamentally performance limiting to the system. Hence we will neglect these aspects in this model.

The final power P_r is obtained after cascaded combining in the individual stages. To distinguish the impact of each receiver aspect we separate the total efficiency η_r into the system sub-efficiencies $\eta_r = \mathrm{CE} \cdot \eta_{tt} \cdot \eta_c$ where CE is the fiber coupling efficiency at perfect tip-tilt-compensation and η_c is the combining efficiency of the entire combining cascade and accounts for the combining efficiency of each sub-stage.

The control system for both the coherent combining and tip-tilt was modelled as a Bang-Bang [32] dither-optical phase locked loop (PLL) [33] using PLL-theory described in [34]. Dither

Optics EXPRESS

PLLs have previously showed outstanding performance in the context of low-SNR phase control [19,33,35] and was also used in our previous demonstration [19]. Exact details of the operation are found in Supplement 1, sect. 4, however, in general, the dither-PLL is optimized using the PLL bandwidth and dither magnitude in order to minimize the phase-error contributions σ_ϕ^2, σ_N^2 and $\sigma_{\phi_d}^2$ from the relative phase ϕ, system noise and phase-dithering, respectively. The contributions of phase and system noise are both calculated from the PLL-filter response to the phase and noise PSDs (based on the PLL bandwidth). While the white system noise PSD is determined by the optical preamplification, input power and dither magnitude, the phase-PSD is generated from the Monte-Carlo simulations we have presently described. The residual phase error after control with the PLL (optimized to the input power and phase PSD) determines the efficiency η_{tt} or η_c (via sub-stage efficiencies) in the case of tip-tilt or coherent combining, respectively.

Each individual efficiency is simulated and investigated with this premise in the respective sections below before the final efficiency is presented in section 6.

3. Coupling efficiency

The fiber coupling efficiency was simulated both with and without tip-tilt-control engaged for the SM and MM receivers for three different turbulence propagation cases (see all parameters in Supplement 1, sect. 2), with coherence lengths r_0 = 10 cm, 20 cm and 60 cm, respectively. To clarify, the coupling efficiency is defined as CE = $P_{\text{fiber}}/P_{\text{aperture}}$ where P_{aperture} is the total power incident on the aperture and P_{fiber} is the power collected by the fundamental mode, for the SM-receiver, or the total power across all fiber modes, for the MM-receiver.

The time-average CE ($\langle$CE$\rangle$) is presented vs. aperture size in Fig. 3 (a) for the SM-receiver and in b) and c) for the MM-receiver using 10 modes and 27 modes, respectively. In a), we see that high coupling efficiency is achieved when $D \lesssim r_0$ with perfect tip-tilt whereas without tip-tilt, high efficiency is limited to $D \lesssim r_0/2$. For increasing D/r_0 ratio, CE drops rapidly which, not surprisingly, effectively limits the efficient use of large size apertures under turbulent conditions. Moreover, the maximum value of CE $\approx$ 0.8 is limited by the mode-matching of a diffraction limited spot to fundamental mode.

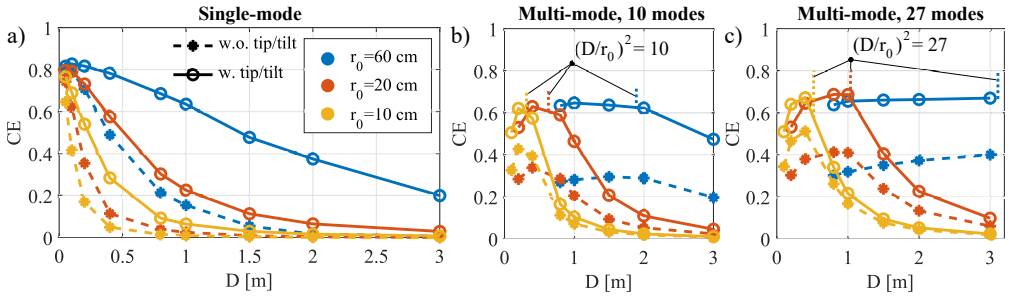

Fig. 3. Simulated coupling efficiency vs. aperture diameter for three different turbulence cases with indicated r_0 values for a) SM-reception, b) MM-reception using the 10 fiber modes indicated in Fig. 2 and c) MM-reception using all 27 modes.

In b) and c), we see that CE remains high as long as the number of collected fiber modes N_f is $\gtrsim (D/r_0)^2$. Here, $N = (D/r_0)^2$ is the number of speckles that fit inside the receiving aperture [36] which typically represent the number of uncorrelated spatial modes received. Our result thus conforms to the principle stating that at least N modes of AO-correction [14,37] or $N_f = N$ fiber modes [38,39] are needed for efficient reception. This result applies to both tip-tilt on and off-cases, although the case with tip-tilt off has overall lower coupling efficiency.

Optics EXPRESS

Based on the conclusions above, that $(D/r_0)^2 \lesssim N_f$ for efficient reception (also for SMF), it appears that the maximum average power that can be efficiently collected per fiber mode is $\approx P_{\text{aperture}}/N = I_r \cdot \pi r_0^2/4$, hence we define a received power per mode as $P_{r_0} = I_r \cdot \pi r_0^2/4$ which allows for easier comparison between different r_0-cases and will be used in the following sections.

4. Tip-tilt compensation

The details for how the tip-tilt compensation can be implemented using a 1st order dither-PLL are described in the supplementary. The result of this model is that AOA-induced focal plane spot-offsets can be converted into a phase ϕ_x as seen by the PLL for the x-direction, similarly for y, when related to the fiber mode-field size. For perfect spot and fiber mode-field matching, the phase is $\propto (D/\lambda)\theta_x$ for the SM-receiver and $\propto (r_0/\lambda)\theta_x$ for the MM-receiver. Here, θ_x is the AOA in the x-direction, y can be treated similarly.

Using the AOA variance $\sigma^2_{\theta_x} \propto (\lambda/D)^2(D/r_0)^{5/3}$ developed in [40] for a receiver in a turbulent channel without tip-tilt compensation, the coupling efficiency degradation from AOA fluctuations can be modelled as

$$\eta_{tt-\text{OFF}} \approx e^{-(\sigma^2_{\phi_x}+\sigma^2_{\phi_y})/2}, \quad \sigma^2_{\phi_x} \propto \left(\frac{D}{r_0}\right)^{5/3} \text{(SM)}, \quad \sigma^2_{\phi_x} \propto \left(\frac{r_0}{D}\right)^{1/3} \text{(MM)}. \tag{1}$$

Here, $\eta_{tt-\text{OFF}}$ represents the minimum tip-tilt efficiency $\min\{\eta_{tt}\}$. This efficiency can be extracted from the results in Fig. 3 as the ratio between CE for the cases with no tip-tilt enabled and perfect tip-tilt compensation. The corresponding ratio is shown in Fig. 4 (a) for the SM and 27-mode MM-receivers (solid) together with fitted theory curves (dashed) given by Eq. (1).

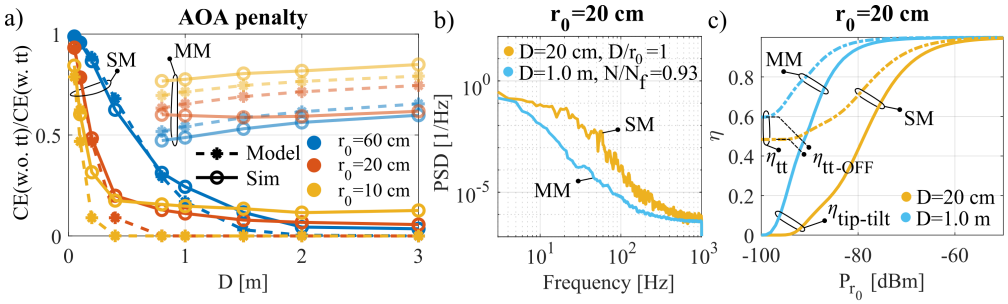

Fig. 4. a) The ratio between CE without and with tip-tilt compensation from Fig. 3 (a) and (c) alongside fitted theoretical curves given by Eq. (1). b) The tip-tilt phase PSD from simulations for the SM and 27-mode MM-receiver with respective aperture size D as indicated. c) The optimized PLL tip-tilt efficiency based on the PSDs in b) and $\eta_{tt-\text{OFF}}$ given by the simulated CE(w.o. tt)/CE(w. tt) shown in a).

Generally, the behaviour of simulation and theory matches, with some discrepancy w.r.t r_0 in the MM case. Significantly, for a given r_0 value, this result shows that larger D reduces the impact of AOA fluctuations (by $\sim D^{-1/3}$) for the MM-receiver (with $f \propto r_0$), whereas for the SM-receiver (with $f \propto D$) the impact of AOA fluctuations is exacerbated (by $\sim D^{5/3}$). This result directly links to the choice of focal lengths for the respective receiver. The reduction of $\sigma^2_{\theta_x}$ with increasing D (aperture averaging) is cancelled by the spot-offset increase due to $f \propto D$ for the SM case whereas it is not for the fixed $f \propto r_0$ in the MM case. As mentioned in the introduction, multi-mode reception alleviates alignment.

The reduced AOA penalty for MM vs. SM receivers is also reflected in the tip-tilt phase PSDs from simulations, with an example shown in Fig. 4 (b), which compares an SM-receiver with $D/r_0 = 1$ and MM-receiver with $N_f/N \approx 1$. Applying an optimized dither-PLL for compensation

Optics EXPRESS

of these phase PSDs results in the tip-tilt efficiency shown in Fig. 4 (c). Here, the tip-tilt efficiencies are related as

$$\eta_{tt} = \eta_{\text{tip-tilt}}(1 - \eta_{tt-\text{OFF}}) + \eta_{tt-\text{OFF}}, \quad \eta_{\text{tip-tilt}} \approx e^{-(\sigma^2_{\phi_{e,x}} + \sigma^2_{\phi_{e,y}})/2}, \tag{2}$$

i.e., $\eta_{\text{tip-tilt}}$ is the locking efficiency of the PLL with residual tip-tilt phase error variances $\sigma^2_{\phi_{e,x}}$ and $\sigma^2_{\phi_{e,y}}$ in x and y, respectively.

The way in which η_{tt} was estimated in the simulation results in erroneous relation between P_{r_0} and simulated η_{tt} for $\eta_{tt}<1$ (the bottom axis of Fig. 4 (c) is actually $\eta \cdot P_{r_0}$), i.e. +1 dB offset in P_{r_0} at $\eta_{tt} = -1$ dB or +3 dB offset at $\eta_{tt} = 0.5$. Despite this limitation, the efficiencies in Fig. 4 (c) provide clear indications of the minimum P_{r_0} required to achieve high η_{tt} for the two receivers. Between the two, the performance of the MM-receiver outperforms the SM-receiver in terms of tip-tilt compensation. This is attributed to the higher input power P for the larger area MM-receiver as well as the smaller tip-tilt phase bandwidth for MM vs. SM-reception as illustrated by the PSDs (thanks to the effect of aperture averaging). In fact, the reduction in η_{tt} for the MM-receiver may be due to reduced combining efficiency η_c, which is shown in later sections to be more limiting than η_{tt} for the MM-receiver.

The tip-tilt efficiencies for SM and MM receivers for other aperture sizes and turbulence cases are presented in the Supplement 1, sect. 8, however, the compared SM and MM-receiver (with $(D/r_0)^2 \approx N_f$) in Fig. 4 b and c) is fairly representative of the optimal multi-aperture and MM receiver configurations, as discussed in later sections.

5. Coherent combining

The overall performance of the combining cascade is heavily dependent on the individual stages, especially the initial combining stage for which the SNR is the lowest, and amplitude and phase fluctuations, typically, the most severe. Here, we begin by considering the performance of the 2-channel combining of adjacent apertures for the SM-receiver. The treatment for coherent combining of modes for the MM-receiver is similar.

5.1. 2-channel combining

Previously in [19] we employed a 1st order dither-PLL for phase compensation for coherent combining. We show in Supplement 1, sect 4C that also amplitude fluctuations can be compensated using a dither-PLL, by re-writing the relative amplitude between channels $r = \sqrt{P_A/P_B}$ as a phase $\phi_r = -\arccos[(1 - r^2)/(1 + r^2)]$. Using this, the compensation of phase and amplitude is accomplished with two independent dither-PLLs optimized toward their respective phase and amplitude-phase PSDs. These PLLs work independently in parallel in each combining stage, see Fig. 2, using the same error feedback port and power detection stage but separated via orthogonal dithers. The resulting combining efficiency of a single stage is (assuming small phase errors)

$$\eta \approx \frac{1}{2}[1 + e^{-(\sigma^2_{\phi_{er}} + R^2\sigma^2_{\phi_e})/2}], \quad R = \frac{2r}{1 + r^2} \tag{3}$$

with $\sigma^2_{\phi_{er}}$ and $\sigma^2_{\phi_e}$ being the residual amplitude-phase and phase error variances, respectively.

Figure 5 shows typical examples of phase PSDs in a) and amplitude-phase PSDs in b) and in c) the combining stage efficiency, corresponding to the PSD in a) (η_a) and b) (η_b), respectively. Additionally, PSDs generated from the Monte-Carlo simulation and analytically modelled phase PSDs for AO systems, based on [26] (see Supplement 1, sect. 5), are compared in a) and show good agreement. Both the PSDs and the efficiency curves, where $\eta_b > \eta_a$ in all cases, indicate relative phase as more performance-limiting for the PLL compared to amplitude variations. We also see that the efficiency degrades with lower power (SNR) and that the PLL sensitivity increases for more severe turbulence cases (shorter r_0). This reflects the trade-off between high PLL-bandwidth

Optics EXPRESS

needed for stronger turbulence and the subsequently reduced SNR ($\propto 1/\text{bandwidth}$). We also note that aperture size impacts both the PSDs and the efficiency in c), where the relative phase between adjacent apertures will be more correlated for $D<r_0$ and less correlated for $D>r_0$.

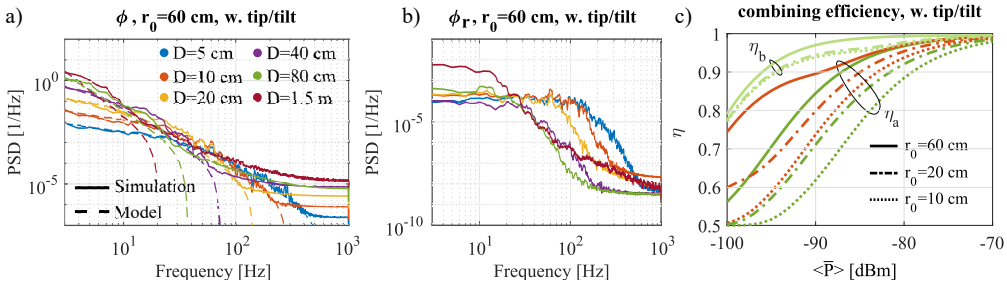

Fig. 5. a) The PSDs of relative phase between adjacent apertures of different size D for the simulated multi-aperture reception in the $r_0 = 60$ cm case. Analytically modelled PSDs based on [26] and Supplement 1 are also included. b) As in a) but for the amplitude-phase PSD. c) The single-stage combining efficiency vs. average input power per channel $\langle \bar{P} \rangle = \langle (P_A + P_B) \rangle / 2$ as limited by relative phase variations η_a ($\sigma^2_{\phi_{er}} = 0$) or by relative amplitude variations η_b ($\sigma^2_{\phi_e} = 0$). Different turbulence cases are indicated via r_0 and two different aperture sizes D are compared (see a)).

The results in Fig. 5 paint a general picture of the single-stage performance. The PSDs as well as η_a and η_b for all $r_0 = [10, 20, 60]$ cm cases can be found in Supplement 1, sect. 8 for both with and without tip-tilt-control. The supplementary also includes the efficiency η_a as generated from the analytically modelled phase PSD which compares well to η_a based on simulated PSDs.

5.2. Experiment

To validate the use of the PLL-model, we conducted a simple 2-channel coherent combining experiment. The details of the experiment are provided in Supplement 1, sect. 6. In short, we used two MEMs-based electrical variable optical attenuators of 1 kHz bandwidth to emulate power fluctuations on either input channel to a combining stage. Phase fluctuations were emulated using phase-shifter ϕ_a (Fig. 2), a piezo-electric fiber stretcher, by adding a noise signal to the phase-compensating signal. The applied phase and power fluctuation voltage signals were generated based on the Monte-Carlo simulations previously described for two turbulence propagation scenarios, representing receiver-sites at La Palma (2.4 km altitude) and Manua Kea (4.4 km altitude) observatories with 60° angle to zenith slant paths. The simulation parameters for these cases were based on measured wind [28] and C_n^2 [41,42] profiles to which we fit the Gaussian wind-profile and Hufnagel-Valley C_n^2 model, respectively (see Supplement 1, sect. 2).

The measured combining efficiency at different dither magnitudes ϕ_d (same for both amplitude and phase compensating PLLs) is compared to the simulated optimal efficiency in Fig. 6 a,b), for the La Palma and Manua Kea cases with $D = 80$ cm. The optimum performance at a given power corresponds to an optimal dither magnitude. By measuring at different dither magnitudes we trace out this optimal performance which compares well with the simulation. The discrepancy at lower powers may be attributed in part to implementation penalties as well as non-negligible natural phase-variations in the fiber-setup that adds to the overall phase noise.

Optics EXPRESS

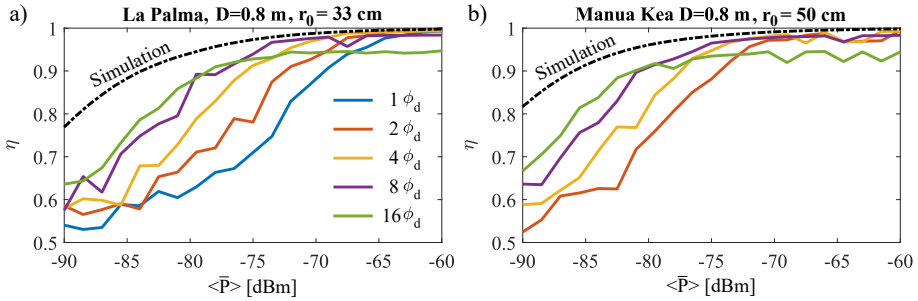

Fig. 6. Comparison of simulated optimal single-stage combining efficiency and measured efficiency for different turbulence cases and aperture sizes. Experimental curves were measured for different dither magnitudes ϕ_d indicated by different colors. a) La Palma case with D = 0.8 m. b) Manua Kea case with D = 0.8 m.

5.3. Multi-channel combining

The resulting combining efficiency from cascaded optical combining is found in [19] and rewritten here using the PLL phase error variance as (assuming small phase errors)

$$\eta_c = \prod_{k=1}^{\log_2(N_c)} \eta_k, \quad \eta_k \approx \frac{1}{2}\left[1 + \exp\left(-\left(\sigma^2_{\phi_{er}} + R^2\sigma^2_{\phi_e} + \sum_{j=1}^{k-1}[\sigma^2_{\phi_{da}}(j) + \sigma^2_{\phi_{db}}(j)]/(4c)^{k-j}\right)/2\right)\right] \quad (4)$$

where N_c is the number of combined channels and c>1/2 (c = 1 for R = 1). By disregarding the sum in the exponential, each subsequent combining stage in the cascade has an efficiency given by Eq. (3). This would be the case in practice if the applied phase dither did not constitute a residual phase perturbation in later stages. The phase error variance contributions $\sigma^2_{\phi_{da}}(j)$, $\sigma^2_{\phi_{db}}(j)$ are that caused by applied dithers in phase shifter ϕ_a and ϕ_b in stage j, previous to current stage k. For a large number of channels, the exponential sum converges to zero in late stages and the impact of dithers on the combined signal will be negligible, a nice scaling feature.

The order in which to combine separate apertures or modes is yet something that can be optimized. However, in this work we investigate only one option in either case. The order in which we combine separate aperture-channels is illustrated in Fig. 7 (a). By implementing the phase compensation in one input arm only (P_A), the output phase of the combining stage will be determined by the other input arm (P_B). Combining apertures according to a) thus maintains the same minimal phase PSD in the first four stages, utilizing any potential coherence between adjacent apertures, before the effective aperture separation (and phase decorrelation) increases. However, since the combined power scales faster than the phase PSD (for larger aperture separation) we expect any reasonable choice of combining order will lead to a final efficiency converging to approximately the same value.

The order of multi-mode combining is illustrated in Fig. 7 (b) for 27 modes and was chosen arbitrarily. The combining order for 6 and 10 modes follow the same approach.

For both the MM and multi-aperture receiver, the overall combining efficiency η_c was calculated using Eq. (4) and for each stage the PLL was optimized with respect to its average input power and phase PSD. The evaluation is thus an iterative process where the input power to the j:th stage depends on the input power to the one before as $P_j(t) = P_{j-1}(t)\eta_{j-1}(t)$. The exact details of how the PSDs for each stage were generated are discussed in Supplement 1, sect. 1. In short, the PSDs for the MM-receiver were also generated iteratively whereas for the multi-aperture combining we relied partially on the analytical Greenwood model for the phase PSD (which compared well to simulations). Here, the same amplitude-phase PSD was used in each stage, although in reality this will reduce in later stages due to the implicit aperture averaging of coherent combining.

Optics EXPRESS

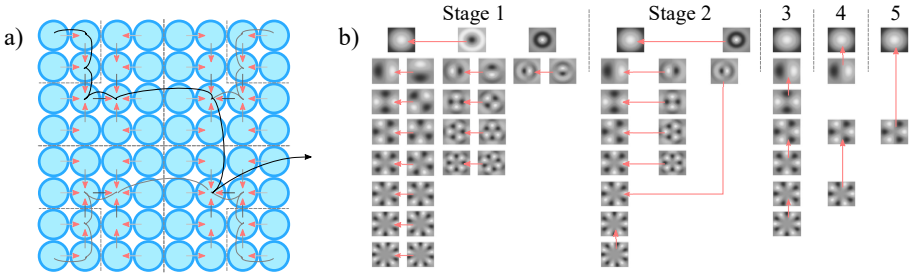

Fig. 7. a) Multi-aperture combining order. b) MM combining order.

This choice, however resulted in similar performance as when the amplitude-phase PSD was completely left out, again illustrating its negligible impact compared to phase.

The number of consecutive stages for the multi-aperture receiver was set to a relatively large number (12), corresponding to $N = 2^{12}$ channels. The large number was chosen to converge the combining efficiency so that comparison between aperture arrays of different size D could be made. The MM-receiver combining efficiency was converged in a similar manner to enable comparison of different aperture sizes as well as to the multi-aperture receiver. This approach allows fair comparison when the number of channels is large $N_c \gg 10$. For fever channels, any difference in channel number or total receive area A_r between cases must be considered.

The performance of the overall combining efficiency for the MM and multi-aperture receivers is summarized by the results in Fig. 8 which shows the total efficiency $\eta_r = \mathrm{CE} \cdot \eta_c$ vs. P_{r_0} in the case with either no implemented tip-tilt or perfect tip-tilt compensation, while excluding the impact of the tip-tilt control system. The inclusion of η_{tt} is covered in the next section.

Figure 8 (a) and b) show η_r (excluding η_{tt}) normalized to the maximum CE for the multi-aperture ($\max\{\mathrm{CE}\} \approx 0.81$) and MM ($\max\{\mathrm{CE}\} \approx 0.69$) receivers, respectively, for the case of $r_0 = 20$ cm, perfect tip-tilt and different D. For the multi-aperture combining we note a trade-off between maximum η_r (dictated by CE, favouring small D) and lower sensitivity (determined by η_c, favouring large D). Based on this result, a good compromise for obtaining both high η_r and low sensitivity for the multi-aperture receiver, is therefore to select $D \approx r_0$ as the optimal configuration. Note also the good agreement between efficiencies based on the simulated and analytically modelled PSDs. For the MM-receiver in b) the optimal choice with regards to both efficiency and sensitivity (no trade-off) is to ensure $N_f \approx N$. These conclusions are also supported by the $r_0 = 10, 60$ cm cases, the results of which are located in Supplement 1, sect. 8.

In the case with no tip-tilt, based on the additional results in the supplementary, it is found that the optimal configuration for the MM-receiver also adhere to $N_f \approx N$ whereas for the multi-aperture receiver $D \approx r_0/2$ provide the best combination of efficiency and sensitivity. These results, for each case of SM or MM reception, with or without tip-tilt, thus match the conditions setup in section 3 for achieving high CE. The optimal choice of D or N_f (considering both efficiency and sensitivity) can thus be intuitively explained by selecting as large aperture D or as few modes N_f as possible while still ensuring a high CE.

Figures 8 (c)-(e) compares η_r for the optimal configuration of the multi-aperture ($D \approx r_0$) and 27-mode MM-receiver ($N_f \approx N$), for the different turbulence cases and with or without tip-tilt compensation. It can be seen that for perfect tip-tilt, the performance of the optimized multi-aperture and MM receivers are very similar. We also see that $D \approx r_0/2$ for the multi-aperture receiver provides better performance than with $D \approx r_0$ or $N \approx N_f$ for the MM-receiver when tip-tilt is off. Note also the ~ 10 dB sensitivity improvement with active tip-tilt compensation.

As we only consider a 27-mode MM-receiver here we cannot simply conclude that multi-aperture reception is superior to MM-reception for tip-tilt off since we could increase D and the

Optics EXPRESS

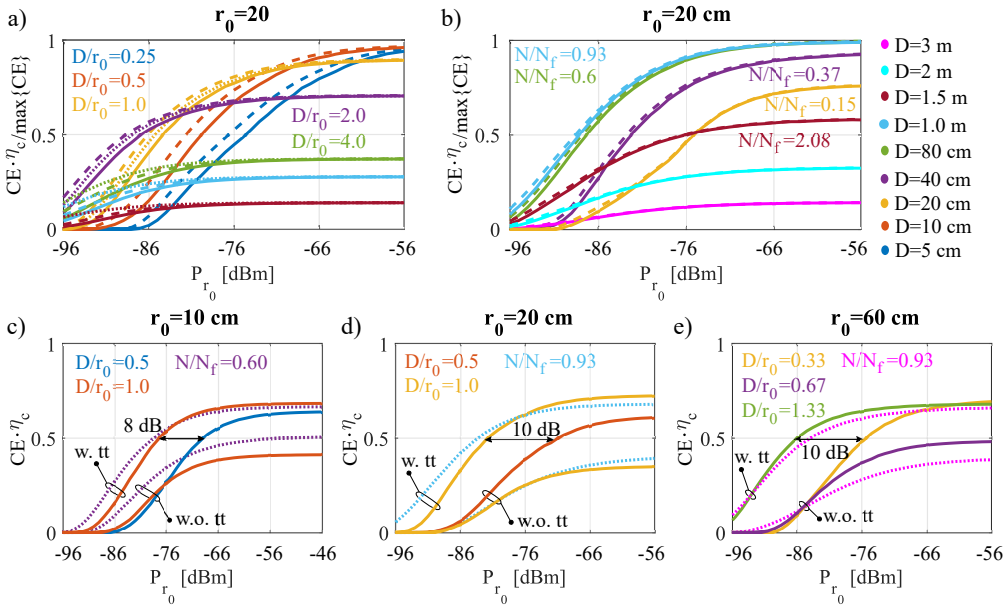

Fig. 8. a) Normalized CE · η_c vs. P_{r_0} for multi-aperture combining for the $r_0 = 20$ cm case with perfect tip-tilt. Dashed and solid lines show the simulated efficiency for η_k given by Eq. (3) and Eq. (4) (with $c = 1/2$), respectively. The dotted line is calculated the same way as the solid line but based on the analytically modelled phase PSDs only. b) As in a) but for the 27-mode MM-receiver. c-e) compare multi-aperture efficiencies (solid) and 27-MM efficiencies (dotted) with η_k based on Eq. (4) ($c = 1/2$) with and without tip-tilt control for the different turbulence cases $r_0 = 10, 20, 60$ cm as indicated.

number of fiber modes (keeping $N_f = N$) to reduce σ_{ϕ_x} from Eq. (1) and improve the tip-tilt efficiency. However, to match halving the aperture size for the SM-receiver $0.5^{5/3}$ it would require increasing the MM-receiver aperture by a factor p such that $1/p^{1/3} = 0.5^{5/3}$, i.e. $p = 2^5$. This would result in $D>f$ for the MM-receiver cases simulated here (for which $f \propto r_0$) which may become physically impractical. As such, due to physical constraints in maintaining a paraxial focusing system, the results indicate the multi-aperture receiver as superior over the MM-receiver when tip-tilt is off for the turbulence cases considered here.

6. Final receiver efficiency

The performance of the final combining efficiency for the MM and multi-aperture SM receivers, this time including η_{tt}, is summarized by the results in Fig. 9 where the optimal multi-aperture and MM-configurations are compared for the different turbulence cases $r_0 = 10, 20, 60$ cm.

We see in figures (a-c) that the final efficiency is almost identical for the MM-receiver when η_{tt} is included or not, across all turbulence cases. This shows that for the MM-receiver (27 modes or more), the combining efficiency η_c has the limiting impact on overall efficiency compared to η_{tt}. This is not the case for the multi-aperture receiver where tip-tilt appear to be performance-limiting with a sensitivity penalty which is larger for larger r_0 values and large D. Hence, when including tip-tilt, the MM-receiver provides better performance than the multi-aperture receiver and offers a few dB better sensitivity for the simulated turbulence cases here.

How the sensitivity varies with turbulence case is emphasized in figure d) and e) for the optimal multi-aperture receiver and in figure f) for the optimal MM-receiver. Although we normalize w.r.t. r_0 by using P_{r_0} we should recall that r_0 does not incorporate the wind speed, instead the

Optics EXPRESS

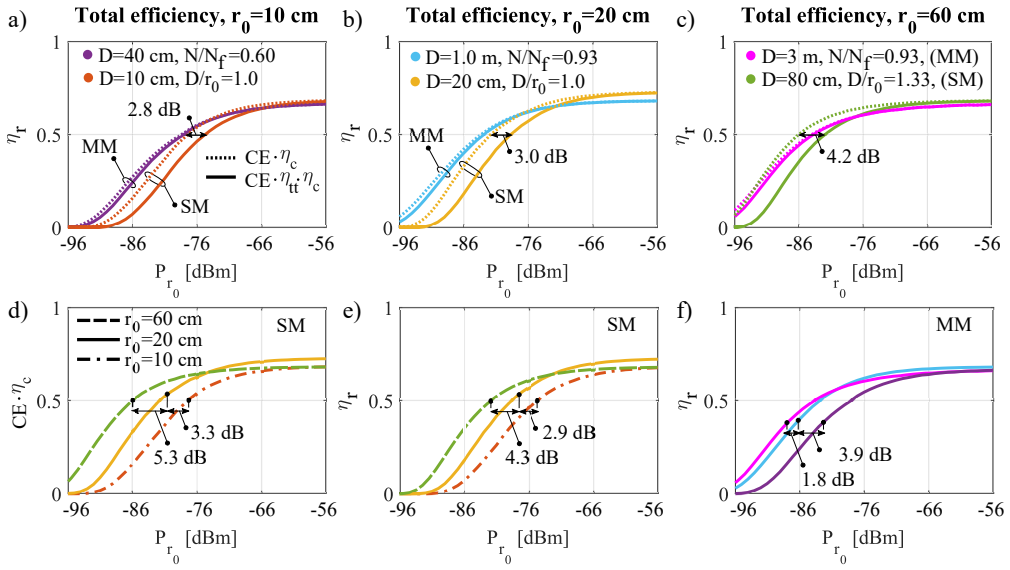

Fig. 9. a-c) The final receiver efficiency vs. P_{r_0} for the optimized receiver configurations for turbulence cases with a) $r_0 = 10$ cm, b) $r_0 = 20$ cm and c) 60 cm. d) Comparison of the receiver efficiency (excluding η_{tt}) between the optimal multi-aperture configuration for each r_0 value. e) As in d) but with η_{tt} included. f) As in e) but for the optimal MM-receiver. All curves displayed here are simulated using η_k from Eq. (4) ($c = 1/2$).

Greenwood frequency f_G [27] provides an estimate for the atmospheric channel bandwidth which for the cases $r_0 = 10, 20, 60$ cm corresponded to $f_G = 68.1, 34.0, 11.3$ Hz, respectively. The larger bandwidth for shorter r_0 explains the reduced sensitivity for these cases.

Unfortunately, we are unable to provide a simple generic model that predicts the sensitivity vs. r_0, D and f_G. Instead, in addition to the specific turbulence cases discussed so far, we present in Fig. 10 the efficiency at two plausible receiver locations, the La Palma and Manua Kea observatory sites discussed in section 5.2. Both turbulence cases use a 60° slant path to zenith and the parameters corresponding to La Palma and Manua Kea are $r_0 = 33$ cm, $f_G = 22.9$ Hz and $r_0 = 50$ cm, $f_G = 10.9$ Hz, respectively.

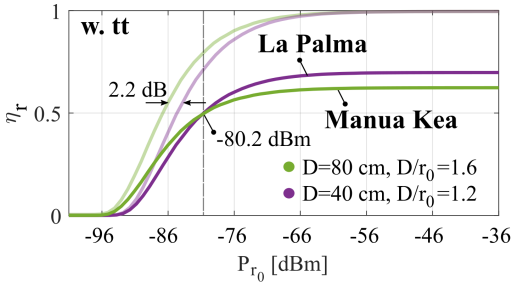

Fig. 10. Final receiver efficiency (including all efficiencies) vs. P_{r_0} of the optimized multi-aperture receiver for the La Palma and Manua Kea turbulence channels. The shaded curves are normalized versions.

Here, only the multi-aperture receiver performance is shown but based on earlier result we can expect the MM-receiver to exhibit a few dB lower sensitivity. From Fig. 10 we estimate

Optics EXPRESS

that efficient reception (η_r>0.5) can be achieved for $P_{r_0} \gtrsim -80 \pm 2$ dBm for both receiver sites, corresponding to an average received intensity of $I_r = 4P_{r_0}/\pi r_0^2$, i.e. -69 ± 2 dBm/m^2 and -73 ± 2 dBm/m^2 for the $D = 40$ cm La Palma and $D = 80$ cm Manua Kea receivers, respectively.

If, for example, error-free optical communication requires $P_r = -59$ dBm of received power (corresponding to 10 Gbaud QPSK error free reception in [11]), a receive-area of $A_r = P_r/I_r\eta_r \approx [20, 50]$ mm^2 would be needed at $\eta_r = 0.5$ and received intensities $[-69, -73]$ dBm/ mm^2. This is equivalent to $A_r/(D^2\pi/4) \approx [160, 100]$ number of $D = [40, 80]$ cm apertures and as many combining stages (minus one) with three times the number of PLL power-detection stages (x1 for combining and x2 for tip-tilt feedback). For an MM-receiver, assuming the same received intensities and η_r the required aperture size would be $D = \sqrt{4A_r/\pi} \approx [5, 8]$ m and a number of fiber modes on the order of $N_f \approx [200, 250]$ with as many combining stages (minus one) and PLL power detection stages. If $D = r_0$ for the considered multi-aperture receivers then the number of apertures and fiber modes in the MM-receivers would be the same.

Other aspects that influence the receiver sensitivity for this system are the optical amplifier noise figure (directly impacts sensitivity) and the $\Delta\nu_o = 27.5$ GHz optical filter in the power detection stage which scales the sensitivity as $\propto \sqrt{\Delta\nu_o}$. A smaller filter bandwidth promotes better sensitivity but can only be as narrow as the symbol rate, hence it can be inferred that the PLL sensitivity scales with the square root of the symbol rate if matched filtering is adopted.

It should also be emphasized that the minimum receive-intensities for efficient reception ($[-69, -73]$ dBm/ mm^2 at $\Delta\nu_o = 27.5$ GHz) is an important constraint for the deep-space link budget and will set a limit to how far away the transmitter can be situated regardless of how large receive area one has, given a specific transmit power and telescope size.

While the estimated values here give and indication toward a practical receiver implementation, it should be noted that the atmospheric channel properties varies throughout the day-night cycle which may result in worse sensitivities w.r.t. I_r during more severe conditions.

Overall we have focused on efficiency in terms of received power per receiver area, however, the receiver cost may be differently distributed w.r.t. to aperture size D and number of PLLs used. To minimize cost while also maximizing area, it may be necessary to do further analysis, where more PLLs may be favoured over expensive large size apertures or the opposite. It should also be noted that there may exist better implementations of tip-tilt compensation than of that presented here, which could both reduce the amount of hardware required (e.g. x2 power detection stages for the SM-receiver) and improve the sensitivity.

7. Discussion and conclusion

We have investigated the multi-aperture and multi-mode receiver architectures together with optical coherent combining for reception of weak optical communications signals with focus on efficiency and sensitivity. We conclude that the rule of thumb when designing the multi-aperture or multi-mode receiver is to ensure $N_f \simeq (D/r_0)^2$, i.e., that the number of fiber modes matches the number modes (or speckles) received by the aperture. This choice will provide as low system sensitivity as possible while still maintaining high receiver efficiency, assuming a system with active tip-tilt control. The implementation of tip-tilt control is found to not only improve the efficiency of reception but also the sensitivity by approximately one order of magnitude.

The performance between the multi-aperture and multi-mode receiver were found to be similar considering coherent combining of channels, however, it was found that tip-tilt control was performance-limiting for the multi-aperture receiver, in contrast to the multi-mode approach. Hence, a few dB better sensitivity can be expected from the use of multi-mode reception for the type of turbulence channels covered here.

For the optically preamplified error feedback dither-PLL investigated here, the simulation results show that receiver efficiencies η_r>0.5 can be achieved for a received power per mode down to -80 ± 2 dBm at plausible high-elevation receiver sites and signal bandwidth up to 25 GHz.

Optics EXPRESS

This translates to received intensities in the range of $[-75, -65] \pm 2$ dBm/m^2 for $r_0 \in (10, 60)$ cm. For the AO demonstration in [14], with aperture size $D = 1$ m and worst case $r_0 = 4.5$ cm, the corresponding power per mode to obtain $\eta_r > 0.5$ would be $P_{r_0} \geq -61$ dBm, which highlights the potential sensitivity boost (on the order of 20 dB) that our investigated receivers could leverage in comparison. However, other sensitive error signal detection schemes, e.g. using single-photon detectors (which would suit this low bandwidth application) may provide even lower sensitivities [43] and could push the low-power limit for efficient reception of weak signals. Meanwhile, an important approach that could enable efficient reception regardless of received signal power is the use of AO together with laser guide stars [44].

Still, among the investigated high sensitivity receiver architectures, the prospect of coherent combining, together with multi-aperture or multi-mode reception, has the potential to enable excellent turbulence mitigation sensitivity for efficient reception of weak signals for future high speed deep-space links which in turn could help relieve the current RF-bottleneck of space communications.

Funding. Vetenskapsrådet (VR-2015-00535).

Acknowledgments. We would like to thank Erik Börjeson for help with FPGA programming and Jason D. Schmidt for discussion on the simulation approach.

Disclosures. The authors declare that there are no conflicts of interest related to this article.

Data availability. Data underlying the results presented in this paper are available in Ref. [45].

Supplemental document. See Supplement 1 for supporting content.

References

1. D. M. Boroson, B. S. Robinson, D. V. Murphy, *et al.*, "Overview and results of the Lunar Laser Communication Demonstration," in *Free-Space Laser Communication and Atmospheric Propagation XXVI*, vol. 8971 H. Hemmati and D. M. Boroson, eds., International Society for Optics and Photonics (SPIE, 2014), p. 89710S.
2. J. P. Laboratory, "Nasa's tech demo streams first video from deep space via laser," WWW page, Accessed: 20240613 (2024). https://www.nasa.gov/directorates/stmd/tech-demo-missions-program/deep-space-optical-communications-dsoc/nasas-tech-demo-streams-first-video-from-deep-space-via-laser/.
3. M. Toyoshima, W. R. Leeb, H. Kunimori, *et al.*, "Comparison of microwave and light wave communication systems in space applications," Opt. Eng. **46**(1), 015003 (2007).
4. S. Shambayati, D. Morabito, J. Border, *et al.*, "Mars reconnaissance orbiter ka-band (32 ghz) demonstration: cruise phase operations," in *SpaceOps 2006 Conference*, (2006), p. 5786.
5. P. I. Hopman, P. W. Boettcher, L. M. Candell, *et al.*, "An end-to-end demonstration of a receiver array based free-space photon counting communications link," in *Free-Space Laser Communications VI*, vol. 6304 A. K. Majumdar and C. C. Davis, eds., International Society for Optics and Photonics (SPIE, 2006), p. 63040H.
6. M. E. Grein, A. J. Kerman, E. A. Dauler, *et al.*, "An optical receiver for the Lunar Laser Communication Demonstration based on photon-counting superconducting nanowires," in *Advanced Photon Counting Techniques IX*, vol. 9492 M. A. Itzler and J. C. Campbell, eds., International Society for Optics and Photonics (SPIE, 2015), p. 949208.
7. R.-J. Essiambre, C. Guo, S. Kanth Dacha, *et al.*, "Record Photon Information Efficiency with Optical Clock Transmission and Recovery of 12.5 bits/photon over an Optical Channel with 77 dB Loss," arXiv, (2023).
8. B. S. Robinson, A. J. Kerman, E. A. Dauler, *et al.*, "781 Mbit/s photon-counting optical communications using a superconducting nanowire detector," Opt. Lett. **31**(4), 444–446 (2006).
9. H. Hao, Q.-Y. Zhao, Y.-H. Huang, *et al.*, "A compact multi-pixel superconducting nanowire single-photon detector array supporting gigabit space-to-ground communications," Light: Sci. Appl. **13**(1), 25 (2024).
10. M. Jarzyna, L. Kunz, W. Zwolinski, *et al.*, "Photon information efficiency limits in deep-space optical communications," Opt. Eng. **63**(04), 041209 (2024).
11. R. Kakarla, J. Schröder, and P. A. Andrekson, "One photon-per-bit receiver using near-noiseless phase-sensitive amplification," Light: Sci. Appl. **9**(1), 153 (2020).
12. D. L. Fried, "Optical resolution through a randomly inhomogeneous medium for very long and very short exposures," J. Opt. Soc. Am. **56**(10), 1372–1379 (1966).
13. C. Rao, L. Zhong, Y. Guo, *et al.*, "Astronomical adaptive optics: a review," PhotoniX **5**(1), 16 (2024).
14. M. W. Wright, J. F. Morris, J. M. Kovalik, *et al.*, "Adaptive optics correction into single mode fiber for a low earth orbiting space to ground optical communication link using the opals downlink," Opt. Express **23**(26), 33705–33712 (2015).
15. W. Guo, Y. Li, J. Chen, *et al.*, "Satellite-to-ground optical downlink model using mode mismatching multi-mode photonic lanterns," Opt. Express **31**(21), 35041–35053 (2023).

Optics EXPRESS

16. D. J. Geisler, T. M. Yarnall, M. L. Stevens, *et al.*, "Multi-aperture digital coherent combining for free-space optical communication receivers," Opt. Express **24**(12), 12661–12671 (2016).
17. C. Geng, F. Li, J. Zuo, *et al.*, "Fiber laser transceiving and wavefront aberration mitigation with adaptive distributed aperture array for free-space optical communications," Opt. Lett. **45**(7), 1906–1909 (2020).
18. Y. Yang, C. Geng, F. Li, *et al.*, "Multi-aperture all-fiber active coherent beam combining for free-space optical communication receivers," Opt. Express **25**(22), 27519–27532 (2017).
19. R. Larsson, J. Schröder, M. Karlsson, *et al.*, "Coherent combining of low-power optical signals based on optically amplified error feedback," Opt. Express **30**(11), 19441–19455 (2022).
20. C. Rao, S. Cui, Y. Tu, *et al.*, "Toward practical digital phase alignment for coherent beam combining in multi-aperture free space coherent optical receivers," IEEE Access **8**, 202585–202595 (2020).
21. C. Ju, N. Liu, D. Wang, *et al.*, "Real-time demonstration of two-aperture coherent digital combining free-space optical transmission with a real-valued mimo adaptive equalizer," Opt. Lett. **49**(4), 903–906 (2024).
22. J. D. Schmidt, *Numerical Simulation of Optical Wave Propagation with Examples in MATLAB* (SPIE, 2010), Chap. 9.
23. L. C. Andrews and R. L. Phillips, *Laser Beam Propagation through Random Media*, 2nd ed. (SPIE, 2005), Chap. 3.
24. Y. K. Chahine, S. A. Tedder, B. E. Vyhnalek, *et al.*, "Beam propagation through atmospheric turbulence using an altitude-dependent structure profile with non-uniformly distributed phase screens," in *Free-Space Laser Communications XXXII*, vol. 11272 H. Hemmati and D. M. Boroson, eds., International Society for Optics and Photonics (SPIE, 2020), p. 1127215.
25. S. Basu, "A simple approach for estimating the refractive index structure parameter (cn2) profile in the atmosphere," Opt. Lett. **40**(17), 4130–4133 (2015).
26. D. P. Greenwood and D. L. Fried, "Power spectra requirements for wave-front-compensative systems*," J. Opt. Soc. Am. **66**(3), 193–206 (1976).
27. D. P. Greenwood, "Bandwidth specification for adaptive optics systems*," J. Opt. Soc. Am. **67**(3), 390–393 (1977).
28. L. C. Roberts and L. W. Bradford, "Improved models of upper-level wind for several astronomical observatories," Opt. Express **19**(2), 820–837 (2011).
29. B. P. Dix-Matthews, S. W. Schediwy, D. R. Gozzard, *et al.*, "Point-to-point stabilized optical frequency transfer with active optics," Nat. Commun. **12**(1), 515 (2021).
30. F. Zou, Z. Pan, J. Liu, *et al.*, "Bidirectional coherent beam combining and turbulence mitigating by phased fiber laser array in a 2 km atmospheric link," Opt. Laser Technol. **163**, 109311 (2023).
31. S. G. Leon-Saval, N. K. Fontaine, J. R. Salazar-Gil, *et al.*, "Mode-selective photonic lanterns for space-division multiplexing," Opt. Express **22**(1), 1036–1044 (2014).
32. M. Zanuso, D. Tasca, S. Levantino, *et al.*, "Noise Analysis and Minimization in Bang-Bang Digital PLLs," IEEE Transactions on Circuits and Systems II: Express Briefs **56**, 835–839 (2009).
33. F. Herzog, K. Kudielka, D. Erni, *et al.*, "Optical phase locking by local oscillator phase dithering," IEEE J. Quantum Electron. **42**(10), 973–985 (2006).
34. J. J. Spilker, *Digital Communications by Satellite* (Prentice-Hall, 1977), Chap. 12, pp. 377–378.
35. R. Larsson, K. Vijayan, and P. A. Andrekson, "Zero-offset frequency locking of lasers at low optical powers with an optical phase locked loop," J. Lightwave Technol. **42**(3), 1183–1190 (2024).
36. Y. Dikmelik and F. M. Davidson, "Fiber-coupling efficiency for free-space optical communication through atmospheric turbulence," Appl. Opt. **44**(23), 4946–4952 (2005).
37. F. Sun, Z. Cao, Y. Wang, *et al.*, "Dm/lcwfc based adaptive optics system for large aperture telescopes imaging from visible to infrared waveband," Opt. Express **24**(24), 27494–27508 (2016).
38. Y. K. Chahine, S. A. Tedder, J. Staffa, *et al.*, "Optimal efficiency for passively coupling partially coherent light intomode-limited optical waveguides," J. Opt. Soc. Am. A **38**(12), 1732–1743 (2021).
39. M. Diab, A. N. Dinkelaker, J. Davenport, *et al.*, "Starlight coupling through atmospheric turbulence into few-mode fibres and photonic lanterns in the presence of partial adaptive optics correction," Mon. Not. R. Astron. Soc. **501**(2), 1557–1567 (2020).
40. G. A. Tyler, "Bandwidth considerations for tracking through turbulence," J. Opt. Soc. Am. A **11**(1), 358–367 (1994).
41. T. Cherubini, S. Businger, and R. Lyman, "Modeling optical turbulence and seeing over mauna kea: Verification and algorithm refinement," J. Appl. Meteorol. Climatol. **47**(12), 3033–3043 (2008).
42. B. García-Lorenzo and J. J. Fuensalida, "Statistical structure of the atmospheric optical turbulence at Teide Observatory from recalibrated generalized SCIDAR data," Mon. Not. R. Astron. Soc. **410**(2), 934–945 (2010).
43. A. Mikos-Nuszkiewicz, J. Paczos, K. Banaszek, *et al.*, "Bayesian approach to coherent combination of single photon beams," Opt. Express **32**(16), 28769–28778 (2024).
44. C. d'Orgeville and G. J. Fetzer, "Four generations of sodium guide star lasers for adaptive optics in astronomy and space situational awareness," in *Adaptive Optics Systems V*, vol. 9909 E. Marchetti, L. M. Close, and J.-P. Véran, eds., International Society for Optics and Photonics (SPIE, 2016), p. 99090R.
45. R. Larsson, M. Karlsson, and P. Andrekson, "Data - Sensitive optical free-space receiver architecture for coherent combining of deep-space communication signals through atmospheric turbulence," Zenodo (2024), https://doi.org/10.5281/zenodo.13858248.